Homogenization based continuum damage mechanics model for monotonic and cyclic damage evolution in 3D composites

Jayesh R. Jain[*] and Somnath Ghosh[‡]

*Computational Mechanics Research Laboratory, Department of Mechanical Engineering,
The Ohio State University, Columbus, OH 43210, USA*

Abstract. This paper develops a 3D homogenization based continuumdamage mechanics (HCDM) model for fiber reinforced composites undergoing micromechanical damage under monotonic and cyclic loading. Micromechanical damage in a representative volume element (RVE) of the material occurs by fiber-matrix interfacial debonding, which is incorporated in the model through a hysteretic bilinear cohesive zone model. The proposed model expresses a damage evolution surface in the strain space in the principal damage coordinate system or PDCS. PDCS enables the model to account for the effect of non-proportional load history. The loading/unloading criterion during cyclic loading is based on the scalar product of the strain increment and the normal to the damage surface in strain space. The material constitutive law involves a fourth order orthotropic tensor with stiffness characterized as a macroscopic internal variable. Three dimensional damage in composites is accounted for through functional forms of the fourth order damage tensor in terms of components of macroscopic strain and elastic stiffness tensors. The HCDM model parameters are calibrated from homogenization of micromechanical solutions of the RVE for a few representative strain histories. The proposed model is validated by comparing results of the HCDM model with pure micromechanical analysis results followed by homogenization. Finally, the potential of HCDM model as a design tool is demonstrated through macro-micro analysis of monotonic and cyclic damage progression in composite structures.

Keywords: continuum damage mechanics; fatigue damage; homogenization; interfacial debonding; cohesive zone element; principal damage coordinate system

1. Introduction

Composite materials are increasingly being used in automobile, aircraft and other high performance applications because of their improved mechanical properties such as high specific stiffness and strength. These structural components are often subjected to complicated cyclic loading history. Although composites may have better fatigue life than metals, deficiencies in current life prediction techniques hinder optimal design of composite structures under cyclic loading. Unlike most metals, fatigue damage in composites starts early and grows steadily with deterioration of stiffness in damaged regions causing redistribution of stresses. As a result, prediction of final failure

---

* Graduate Research Associate
‡ Corresponding Author, John B. Nordholt Professor, Tel: +1 614 292 2599, Email: ghosh.5@osu.edu

requires complete simulation of cyclic damage progression in the structure. Conventional fatigue life approaches characterize the fatigue damage by macroscopic quantities such as stress/strain and experimentally obtained fatigue life or fatigue strength. Popular approaches for fatigue in metals include stress-life for High Cycle Fatigue (HCF), strain-life for Low Cycle Fatigue (LCF) and several other models based on S-N or Goodman type diagrams, described in Suresh (1996). These concepts have been extended to composites by Hashin & Rotem (1973), Gathercole *et al.* (1994) and others (Degrieck & Paepegem 2001). These total life approaches, however, do not take into account the actual damage mechanisms such as localized cyclic plastic strains in metals or matrix/interfacial cracks in composites, rendering them empirical in nature.

Experimental investigations have shown reduction in the elastic stiffness during fatigue damage progression in fiber-reinforced composites (Talreja 1987, Reifsnider 1987). Phenomenological models have been proposed in the literature characterizing fatigue damage through stiffness degradation, (e.g. Sidoroff & Subagio 1987, Whitworth 1998). In this regard, continuum damage mechanics (CDM) models provide a constitutive framework for reflecting damage induced stiffness reduction with the introduction of effective damage parameters that represent overall material degradation (Kachanov 1987, Voyiadjis & Kattan 2006, Krajicinovic 1996). Damage and failure of composite materials are inherently multiple scale phenomena coupling different scales of damage initiation and progression. Two types of CDM models, viz. phenomenological and micromechanical models, have been proposed in the literature for modeling failure of composite materials. The phenomenological CDM models (Chaboche 1981, Simo & Ju 1987, Chow & Wang 1987, Arnold & Kruch 1991, Bhattacharya & Ellingwood 1999, Chow & Wei 1999, Desmorat *et al.* 2007) employ scalar, second order and fourth order damage tensors using mathematically and thermodynamically consistent formulations of damage mechanics. Damage parameters are identified through macroscopic experiments and in general, they do not explicitly account for damage mechanisms in the microstructure. In Desmorat *et al.* (2007), a generalized damage law has been developed in terms of cumulative measure of internal sliding for monotonic, hysteretic, dynamic and cyclic loading without explicit consideration of micromechanics. Micromechanics based approaches (Fish *et al.* 1999, Chaboche *et al.* 1998, Ladeveze 2002, Ju *et al.* 2006, Akshantala & Talreja 2000, Ladeveze 2002, Echle & Voyiadjis 1999, Fish & Yu 2002, Kruch *et al.* 2006, Rosek & Onate 2008), on the other hand conduct micromechanical analysis of a representative volume element (RVE) with subsequent homogenization, to predict evolving material damage behavior. The CDM model in Echle & Voyiadjis (1999) employs kinematic hardening type damage surface in stress space to account for cyclic damage. In Fish & Yu (2002), the damage surface concept is dropped and loading/unloading during fatigue is determined based on equivalent strain. An arc-tangent form of evolution law for scalar damage evolution is assumed in this case. With the exception of a few (e.g. Voyiadjis & Kattan 2006, Fish *et al.* 1999, Kouznetsova *et al.* 2001, Raghavan & Ghosh 2005), most damage models do not account for the evolution of damage or the effect of loading history. Significant error can consequently accrue in the solution of problems, especially those that involve non-proportional loading. Some of these homogenization studies have overcome this shortcoming through the introduction of simultaneous RVE-based microscopic and macroscopic analysis in each load step (Fish *et al.* 1999, Feyel & Chaboche 2000). However, such approaches can be computationally expensive, especially during fatigue, since detailed micromechanical analyses need to be conducted in each load step at every integration point in elements of the macroscopic structure.

To overcome the shortcomings of macro-micro modeling of composites for predicting damage,

Ghosh and coworkers (Raghavan & Ghosh 2005, Ghosh *et al.* 2007) have developed a computationally efficient, anisotropic homogenization based continuum damage mechanics (HCDM) model for composites undergoing microstructural damage. Specifically fiber-matrix interface debonding has been taken as the microstructural damage mechanism in these two dimensional analyses, for which micromechanical analyses are conducted by the Voronoi cell FEM model (Li & Ghosh 2004). This model is constructed by homogenizing evolving damage variables in micromechanical analyses of a representative microstructural volume element of the composite. The homogenization based continuum damage model (HCDM) has been successfully used for macroscopic analysis in multi-scale modeling of composites undergoing fiber-matrix interfacial debonding in Ghosh *et al.* (2007). In a multi-scale modeling framework, the use of a continuum damage mechanics model in regions of non-critical diffused damage evolution makes the overall computing extremely efficient. This model can avoid the need to perform micromechanical analysis at each load increment. However, it is necessary to zoom into the microstructure and perform pure microscopic analysis in critical regions of dominant crack propagation or localized instability to accurately predict catastrophic failure (Ghosh *et al.* 2007).

The 2D HCDM model in Raghavan & Ghosh (2005) does not incorporate the effects of the path dependent load history on the parameters in the damage model. Hence its predictions are not accurate for e.g., non-proportional loading cases. The authors have developed a 3D HCDM model in Jain & Ghosh (2008b,a) that overcomes these limitations through the introduction of a principal damage coordinate system (PDCS), which evolves with the load history. The objective of the present work is to develop a unified continuum damage modeling framework that employs same damage evolution law for monotonic as well as fatigue damage. To account for fatigue damage, loading/unloading criterion based on scalar product of the normal to the damage surface in strain space and the applied strain increment is proposed. A similar criterion has been used in Marigo (1985) to develop a phenomenological fatigue damage law. The 3D HCDM model introduces functional forms of a fourth order damage tensor in terms of macroscopic strain and stiffness tensor components that are calibrated by micromechanical RVE analysis along different strain loading paths. Anisotropy and its evolution are also effectively treated in this model. Parametric representation of various damage tensors significantly enhances the computational efficiency by avoiding cumbersome strain space interpolations in Raghavan & Ghosh (2005). The HCDM model can be conveniently incorporated in any finite element code, e.g., ABAQUS or MARC for efficient modeling of damage evolution in composite structures due to degrading microstructures.

The CDM model proposed has two main attributes. It has a very strong connection with the micromechanical phenomena. For example, one can relate the macroscopic damage energy to the amount of debonding or fiber cracking in the microstructure for any composite architecture. Thus, it can be used as an effective tool for microstructure design. The second is that the CDM model overcomes the necessity for tedious micro-macro computations, while getting the same accuracy and dependence on the microstructure and micromechanics. Hence it can be coupled and used in any commercial software for macro-scale structural analyses.

This paper starts with a brief overview of continuum damage mechanics and establishes significance of PDCS in section 2. Section 3 describes the micromechanical model with interfacial debonding followed by its homogenization. An orthotropic homogenization based CDM or HCDM model developed in the PDCS is discussed in section 4. This section also discusses parameter calibration for monotonic and cyclic loading. Section 5 provides the stress update procedure with HCDM in its implementation in a macroscopic finite element code for structural analysis. Validation

of the HCDM model for a single fiber RVE subjected to monotonic and cyclic loading is presented in section 6. Section 7 presents demonstrative structural applications to show the capabilities of the HCDM model. The paper concludes with a brief summary of the developed model.

2. Anisotropic continuum damage mechanics

The general form of CDM models (see e.g. Kachanov 1987), introduces a fictitious stress $\tilde{\Sigma}_{ij}$ acting on an effective resisting area ($\tilde{A}$). This is caused by reduction of the original resisting area A due to material degradation due to the presence of micro-cracks and stress concentration in the vicinity of cracks. In Raghavan & Ghosh (2005), Simo & Ju (1987), the effective stress $\tilde{\Sigma}_{ij}$ is related to the actual Cauchy stress Σ_{ij} through a fourth order damage effect tensor M_{ijkl} as

$$\tilde{\Sigma}_{ij} = M_{ijkl}(\mathbf{D})\Sigma_{kl} \qquad (1)$$

where M_{ijkl} is a function of a damage tensor $\mathbf{D}$ ($= D_{ijkl}\mathbf{e_i} \otimes \mathbf{e_j} \otimes \mathbf{e_k} \otimes \mathbf{e_l}$). $\mathbf{D}$ can be a zero-th, second or fourth order tensor, depending on the model employed. As discussed in Voyiadjis & Kattan (2006), Cordebois & Sidoroff (1982), the hypothesis of equivalent elastic energy is used to evaluate M_{ijkl} and establish a relation between the damaged and undamaged stiffnesses as

$$W_C(\Sigma, \mathbf{D}) = \frac{1}{2}(E_{ijkl}(\mathbf{D}))^{-1}\Sigma_{ij}\Sigma_{kl} = W_C(\tilde{\Sigma}, \mathbf{0}) = \frac{1}{2}(E^o_{ijkl})^{-1}\tilde{\Sigma}_{ij}\tilde{\Sigma}_{kl} \qquad (2)$$

where $\Sigma = \Sigma_{ij}\mathbf{e_i} \otimes \mathbf{e_j}$, E^o_{ijkl} is the elastic stiffness tensor in the undamaged state and $E_{ijkl}(\mathbf{D})$ is the stiffness in a damaged state. From Eqs. (1) and (2), the relation between the damaged and undamaged stiffnesses is established as

$$E_{ijkl} = (M_{pqij})^{-1}E^o_{pqrs}(M_{rskl})^{-T} \qquad (3)$$

where the exponent $-T$ corresponds to the transpose of the inverse of the fourth order $\mathbf{M}$ tensor. With the choice of an appropriate order of the damage tensor and the assumption of a function for M_{ijkl}, Eq. (3) can be used to formulate a damage evolution model using micromechanics and homogenization.

2.1 Principal damage coordinate system (PDCS)

For a second order damage tensor D_{ij}, the damage effect tensor M_{ijkl} in Eq. (1) has been formulated in Murakami (1988) as:

$$M_{ijkl} = (\delta_{ik} - D_{ik})^{-1}\delta_{jl} \qquad (4)$$

D_{ij} is symmetric and it can describe the damage states which have at least orthotropic symmetry. For any arbitrary D_{ij} the corresponding effective stress tensor, obtained by substituting Eq. (4) in Eq. (1), may be unsymmetric. An implicit method of rendering the stress tensor symmetric has been suggested in Voyiadjis & Kattan (2006), which is used to derive the inverse of the damage effect tensor $[\mathbf{M}(D_{ij})]^{-1}$. The present work assumes orthotropy of the homogenized stiffness matrix in the principal damage coordinate system. For known values of E^o_{ijkl} and E_{ijkl}, Eq. (3) results in a system of nonlinear algebraic equations in D_{ij}, which are solved by nonlinear least squares minimization. Subsequently, the eigen-vectors of D_{ij}, viz. $\mathbf{e_{D1}}$, $\mathbf{e_{D2}}$ and $\mathbf{e_{D3}}$ are evaluated and the transformation

matrix $[\mathbf{Q}]^D = [\mathbf{e_{D1}} \; \mathbf{e_{D2}} \; \mathbf{e_{D3}}]^T$ is formed. The rotation matrix $[\mathbf{Q}]^D$ transforms the global coordinate system to the principal damage coordinate system.

2.2 Evolution of PDCS for different load histories

To examine the evolution of PDCS with different load histories, micromechanical analysis of RVE with a single fiber of 20% volume fraction is conducted. To allow debonding, the fiber-matrix interface is modeled using cohesive zone elements as discussed in section 3. Micromechanical analysis is followed by homogenization to evaluate evolving stiffnesses and PDCS in the composite. Two combined loading histories are considered for the analyses: *Case a*: Proportional and *Case b*: Non-proportional. The final state of the macroscopic strain e_{ij} is identical for both the cases. For the proportional loading case (a), the orientation of the damage axes jumps to and remains unchanged at 24° with respect to the global axes throughout damaging process. For the non-proportional loading case (b), the PDCS coincides with the global coordinate system in simple tension during the first half of loading. In the last half of the loading, the PDCS continuously rotates to a final position of 21° orientation. Certainly in this case, the PDCS rotation should be incorporated in the HCDM model to account for the damage history.

3. Micromechanical RVE model and homogenization

3.1 Cohesive zone model for interfacial debonding

A 3D micromechanical model for composite microstructures undergoing fiber-matrix interfacial debonding has been developed in Swaminathan *et al*. (2006) based on bilinear cohesive law. The model has been extended in Bhatnagar *et al*. (2007) to include irreversible hysteretic effects in mixed-mode failures. In this work, the hysteretic bilinear cohesive zone model is employed to simulate fiber-matrix interfacial debonding with fatigue damage accumulation.

In the bilinear cohesive zone element of Swaminathan *et al*. (2006), the relation between traction $T(= \sqrt{T_n^2 + T_{t1}^2 + T_{t2}^2})$ and the effective opening displacement $\delta(= \sqrt{\delta_n^2 + \beta^2 \delta_t^2})$ is given as

$$T = \begin{cases} \dfrac{\sigma_{\max}}{\delta_c}\delta & \text{if } \delta \leq \delta_c \quad \text{(hardening region)} \\[2ex] \dfrac{\sigma_{\max}}{\delta_c - \delta_e}(\delta - \delta_e) & \text{if } \delta_c < \delta \leq \delta_e \quad \text{(softening region)} \\[2ex] 0 & \text{if } \delta > \delta_e \quad \text{(complete debonding)} \end{cases} \tag{5}$$

where (T_n, T_{t1}, T_{t2}) are normal and tangential components of the interfacial traction, $(\delta_n, \; \delta_t = \sqrt{\delta_{t_1}^2 + \delta_{t_2}^2})$ are displacement jumps in normal and tangential directions respectively and β is an empirical factor.

For a positive normal displacement δ_n, the traction at the interface increases linearly to a maximum value of $\sigma_{\max}$ corresponding to δ_c. After that, the traction starts decreasing with increasing separation and finally reaches zero at a value of δ_e. The unloading behavior in the hardening region

follows the same slope as that of the loading path. In the softening region, unloading is assumed to follow a linear path back from the current position to the origin with a reduced stiffness.

Reloading follows the unloading slope till it meets the point of unloading in the softening plot, and then continues along the softening plot. When the normal displacement is negative, stiff penalty springs are introduced to prevent penetration. Details of the implementation of 3D cohesive zone elements in the user defined element (UEL) subroutine of FE code ABAQUS has been discussed in Swaminathan *et al.* (2006).

To account for dissipative mechanisms in the fracture process zone ahead of the crack tip in cyclic loading, the hysteretic model incurs fatigue damage during reloading. Unloading is still assumed to be linearly elastic towards the origin of traction-separation curve. During reloading the cohesive spring stiffnesses in normal and tangential directions are assumed to decay according to the stiffness degradation law given by:

$$\dot{K} = \begin{cases} -K\dfrac{\dot{\delta}}{\delta_f} & \text{if } \dot{\delta} > 0 \\ 0 & \text{if } \dot{\delta} \leq 0 \end{cases} \tag{6}$$

where the material parameter δ_f governs the rate of stiffness decay during cyclic loading. The hysteretic response of the cohesive model remains within the envelope of the bilinear model. When the reloading curve intersects the softening curve, it follows the curve and accrues only monotonic damage as illustrated in Fig. 2. Further details of numerical implementation of the hysteretic cohesive zone element are discussed in Bhatnagar *et al.* (2007).

3.2 Homogenization and stiffness evaluation

Components of the homogenized elastic stiffness tensor E_{ijkl}, are calculated by solving six independent micromechanical boundary value problems of the RVE. The RVE is each case is subjected to periodicity displacement conditions on the boundary. For a given macroscopic or average strain e_{ij}, the corresponding nodes of opposite faces (say n_1^p and n_2^p) of the RVE are constrained as Pellegrino *et al.* (1999)
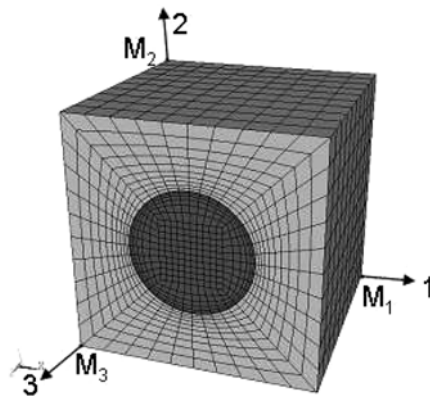

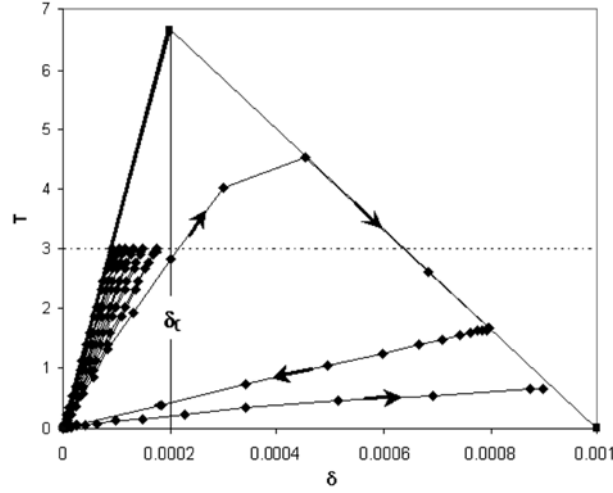Fig. 1 Finite element mesh for the RVE with a cylindrical fiber

Fig. 2 Hysteretic cohesive zone model response under cyclic loading to eventual failure

$$(u_i)_{n_2^p} - (u_i)_{n_1^p} = e_{ij}\Delta x_j \tag{7}$$

where Δx_i are the relative coordinates of nodes on opposite faces. Macroscopic strains are then applied by fixing a corner node and specifying the displacement on master nodes M_1, M_2 and M_3 that belong to orthogonal faces as shown in Fig. 1. Elastic stiffness E_{ijkl} is evaluated by applying single unit strain components to the RVE. These correspond to six boundary value problems, for example, $e_{11} = 1.00$, all other components $= 0$ etc. Finally, the homogenized or macroscopic stresses Σ_{ij} and strains e_{ij} are obtained by volume averaging.

4. Evolution equations for the HCDM model

The anisotropic CDM model involving fourth order damage tensor, proposed in Raghavan & Ghosh (2005), introduces a damage evolution surface to delineate the interface between damaged and undamaged domains in the strain-space (e_{ij}). In this work, a damage evolution surface that is valid for monotonic as well as cyclic loading is written in the principal damage coordinate system (PDCS) as

$$F' = \frac{1}{2}e'_{ij} P'^{m/f}_{ijkl} e'_{kl} - \kappa'(\alpha W_d) \tag{8}$$

where the m/f in the superscript denote monotonic and cyclic loading respectively. W_d is the dissipation of the strain energy density due to stiffness degradation that is expressed as:

$$W_d = \int \frac{1}{2}e'_{ij}e'_{kl} \, dE'_{ijkl} \tag{9}$$

where the prime in the superscript denotes quantities expressed in the PDCS using the transformation laws

$$E'_{ijkl} = Q_{ip}Q_{jq}Q_{kr}Q_{ls}E_{pqrs} \text{ and } e'_{ij} = Q_{ik}Q_{jl}e_{kl} \qquad (10)$$

and Q_{ij} is the transformation matrix. $P'^{m/f}_{ijkl}$ is a fourth order symmetric negative definite tensor that corresponds to the direction of the rate of stiffness degradation tensor $\dot{E}'_{ijkl}$, $\kappa'(\alpha W_d)$ is a damage state variable and α is a scaling parameter.

Damage evolution due to monotonic loading takes place when $F' > 0$. In this case, consistency condition $F' = 0$ is satisfied and assuming associativity rule in the stiffness space, the rate of stiffness degradation in PDCS is given as

$$\dot{E}'_{ijkl} = \lambda \frac{\partial F'}{\partial \left(\frac{1}{2} e'_{ij} e'_{kl} \right)} = \lambda P'^{m}_{ijkl} \qquad (11)$$

The loading/unloading criterion during cyclic loading is based on the inner product of the strain increment $\dot{e}_{ij}$ and the normal to the strain space damage surface $\frac{\partial F'}{\partial e'_{ij}}$. Thus,

$$F' < 0 \quad \frac{\partial F'}{\partial e'_{ij}} \dot{e}'_{ij} > 0 \quad \text{cyclic Damage}$$

$$F' < 0 \quad \frac{\partial F'}{\partial e'_{ij}} \dot{e}'_{ij} = 0 \quad \text{Neutral Loading} \qquad (12)$$

$$F' < 0 \quad \frac{\partial F'}{\partial e'_{ij}} \dot{e}'_{ij} < 0 \quad \text{Unloading}$$

In this case, the damage evolution takes place satisfying the condition $F' < 0$, $\dot{F}' = 0$. The corresponding rate of stiffness degradation in PDCS is

$$\dot{E}'_{ijkl} = \lambda \frac{\partial F'}{\partial \left(\frac{1}{2} e'_{ij} e'_{kl} \right)} = \lambda P'^{f}_{ijkl} \qquad (13)$$

4.1 Parametric forms and parameter calibration

4.1.1 Damage state variable κ'

The damage function $\kappa'(W_d)$ is evaluated for a reference loading path, and results for all other strain paths are scaled with respect to this reference value. For the reference loading path ($e'_{11} \neq 0$, all other $e'_{ij} = 0$), setting $P'_{1111} = 1$, κ' is determined from damage surface of Eq. (8) as

$$\kappa' = \frac{1}{2}(e'_{11})^2 \qquad (14)$$

The function $\kappa'(W_d)$ is determined from the micromechanical analysis by evaluating W_d at each strain increment. The $\kappa' - W_d$ plots for four different strain paths are shown with circular marks in Fig. 3. W_d remains zero in these plots, till κ' exceeds a threshold value corresponding to the initiation of debonding induced microscopic damage. Subsequently, W_d increases rapidly, signaling substantial material deterioration during the initial stages of damage. Eventually, W_d saturates at a
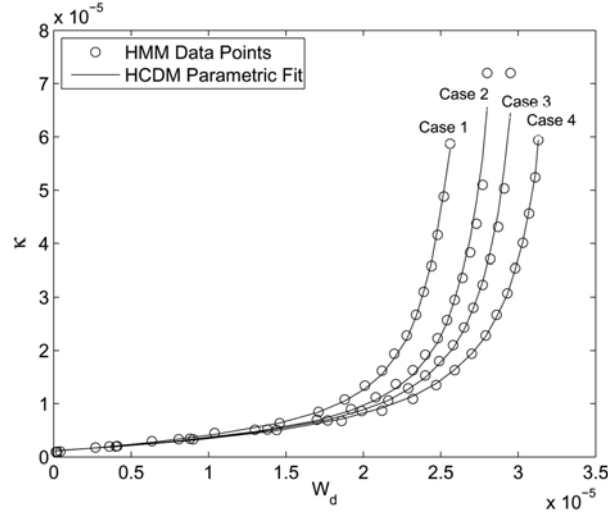
Fig. 3 Functional representation of the $\kappa' - W_d$ relation from homogenized micromechanics (HMM) data points

value W_d^F corresponding to configuration with arrested debond or fully debonded interface. Very little material degradation due to damage occurs beyond this saturation value. The behavior of the plots are similar; however the value of W_d^F differs for the different strain histories. The variability of W_d^F with different loading paths in the 3D strain space can be taken into account using the scaling factor (e_{ij}) as reported in Raghavan & Ghosh (2005). However, such an approach requires evaluation and storage of (e_{ij}) for a large number of individual loading paths for interpolation.

To avoid this approach in the 3D analysis, novel functional forms of κ' are introduced to explicitly describe its dependence on the macroscopic strain components e_{ij}, as well as on W_d. Three invariant forms of the strain components, consistent with anisotropic material properties model are used in these functions. They are:

$$I_1 = \frac{1}{3}(A e_{11} + B e_{22} + C e_{33})$$

$$J_2 = F(e_{22}^d - e_{33}^d)^2 + G(e_{33}^d - e_{11}^d)^2 + H(e_{11}^d - e_{22}^d)^2 + L(e_{12}^d)^2 + M(e_{13}^d)^2 + N(e_{23}^d)^2$$

$$J_3 = O(e_{11}^d e_{22}^d e_{33}^d) + P(e_{11}^d (e_{23}^d)^2) + Q((e_{12}^d)^2 e_{33}^d) + R(e_{13}^d e_{12}^d e_{23}^d) + S((e_{13}^d)^2 e_{22}^d) \tag{15}$$

where $e_{ij}^d = e_{ij} - 1/3 \delta_{ij} e_{kk}$ is the deviatoric strain tensor. The invariants I_1, J_2 and J_3 are respectively linear, quadratic and cubic functions of e_{ij}. The constants A, B, C, F, G, ..., S are introduced to characterize the state of anisotropy in the damaged material. The functional form of κ' is developed to conform to the plots of Fig. 3, and is expressed as:

$$\kappa'(I_1, J_2, J_3, W_d) = b_0 + f(I_1, J_2, J_3)\, [1 + b_1 \tan(b_2 W_d)] \tag{16}$$

The form decomposes its dependence on the dissipation energy and the strain. The latter dependence is represented by a polynomial function of the invariants as:

$$f(I_1, J_2, J_3) = \alpha_0 + \alpha_1 I_1 + \alpha_2 J_2 + \alpha_3 J_3 + \alpha_4 I_1^2 + \alpha_5 I_1 J_2 + \ldots \tag{17}$$

The constants A, B, C, ... in Eq. (15), b_0, b_1, b_2 in Eq. (16), and α_0, α_1, ... in Eq. (17) are determined by a nonlinear least squares minimization of the difference between results of micromechanical analysis and those from the functional form in Eq. (16), i.e.,

$$minimize \sum_{i=1}^{N_{ref}} [\kappa'_{ref} - \kappa'(I_1, J_2, J_3, W_d)]_i^2 \tag{18}$$

Micromechanical analysis of the RVE is conducted for N_{ref} different strain histories to explicitly compute the values of κ'_{ref}. A sufficient number of reference strain paths (N_{ref}) are selected such that the parametric representation in Eq. (16) represents all possible strain history in field simulations. A fifth order polynomial function in Eq. (17) yields good convergence properties for the least square residual. Fig. 3 satisfactorily compares the $\kappa' - W_d$ plots by the function in Eq. (16) with results from the micromechanical analysis for the different strain paths.

4.1.2 Damage surface parameter P'^m_{ijkl} for monotonic loading

In the incremental finite element formulation for evolving damage, the backward Euler method is used to integrate the rate of stiffness degradation in Eq. (11). Corresponding to the strain increment from step n to step $n + 1$, the parameter P'^m_{ijkl} may be expressed as

$$(P'^m_{ijkl})_{n+1} = \frac{(E'_{ijkl})_{n+1} - (E'_{ijkl})_n}{\lambda_{n+1} - \lambda_n} \tag{19}$$

where $(E'_{ijkl})_{n+1}$ is the secant stiffness at the end of the increment. Substituting this into the damage evolution Eq. (8) at the end of the increment yields the incremented form of the damage surface as

$$\frac{1}{2}(e'_{ij})_{n+1}\left(\frac{(E'_{ijkl})_{n+1} - (E'_{ijkl})_n}{\lambda_{n+1} - \lambda_n}\right)(e'_{kl})_{n+1} - \kappa'_{n+1} = 0 \tag{20}$$

where $\kappa'_{n+1}(I_1, J_2, J_3, W_d)$ represents the size of the parametric damage surface and $(W_d)_{n+1}$ at the end of the interval is evaluated by using the backward Euler integration method. The parameter λ_{n+1} is then evaluated from the relation

$$\lambda_{n+1} = \lambda_n + \frac{\frac{1}{2}(e'_{ij})_{n+1}((E'_{ijkl})_{n+1} - (E'_{ijkl})_n)(e'_{kl})_{n+1}}{\kappa'_{n+1}} \tag{21}$$

$(P'^m_{ijkl})_{n+1}$ may be subsequently determined from Eq. (19). The direction of the rate of stiffness degradation varies continuously with damage evolution with increasing loads. From Eq. (11) this implies that P'^m_{ijkl} also varies accordingly. A polynomial function form is derived for the components P'^m_{ijkl} in terms of the anisotropic invariants of strain defined in Eq. (15), as

$$P'^m_{ijkl}(I_1, J_2, J_3) = c_0^{ijkl} + c_1^{ijkl} I_1 + c_2^{ijkl} J_2 + c_3^{ijkl} J_3 + c_4^{ijkl} I_1^2 + c_5^{ijkl} I_1 J_2 + \cdots \tag{22}$$

Again, the coefficients c_p^{ijkl} in Eq. (22) are determined by a nonlinear least square equation solver. Fig. 4(a) shows a comparison of the micromechanical results and the calibrated function in Eq. (22)
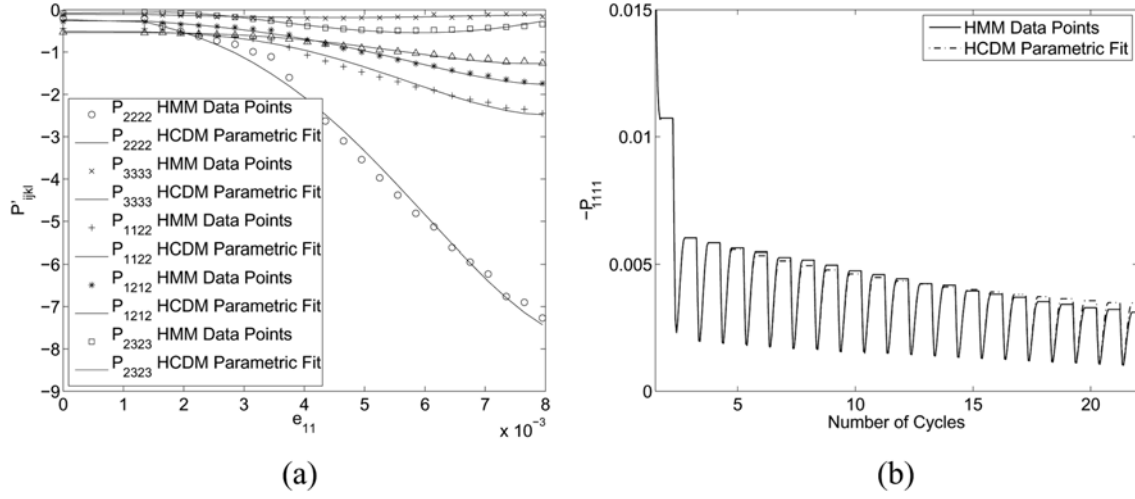
(a)   (b)

Fig. 4 Functional representation of (a) $P'^{m}_{ijkl} - e_1$ and (b) $P'^{f}_{1111} - \dot{e}_{11}$ relations for uniaxial tension from homogenized micromechanics (HMM) data points

for an RVE under uniaxial tension. With a fifth order polynomial function (22), the root mean square error is observed to be less than 3%.

4.2.3 Damage surface parameter P'^{f}_{ijkl} for cyclic loading

Integrating the rate of stiffness degradation in Eq. (13) using backward Euler method, P'^{f}_{ijkl} may be expressed as

$$(P'^{f}_{ijkl})_{n+1} = \frac{(E'_{ijkl})_{n+1} - (E'_{ijkl})_n}{\lambda_{n+1} - \lambda_n} \tag{23}$$

Substituting this into the rate form $\dot{F} = 0$ of damage evolution Eq. (8) yields

$$\frac{1}{2}(e'_{ij})_{n+1}\left(\frac{(E'_{ijkl})_{n+1} - (E'_{ijkl})_n}{\lambda_{n+1} - \lambda_n}\right)(e'_{kl})_{n+1} - \frac{1}{2}(e'_{ij})_n(P'^{f}_{ijkl})_n(e'_{kl})_n - (\kappa'_{n+1} - \kappa'_n) = 0 \tag{24}$$

The parameter λ_{n+1} is then evaluated as

$$\lambda_{n+1} = \lambda_n + \frac{\frac{1}{2}(e'_{ij})_{n+1}((E'_{ijkl})_{n+1} - (E'_{ijkl})_n)(e'_{kl})_{n+1}}{\frac{1}{2}(e'_{ij})_n(P'^{f}_{ijkl})_n(e'_{kl})_n - (\kappa'_{n+1} - \kappa'_n)} \tag{25}$$

$(P'^{f}_{ijkl})_{n+1}$ may be subsequently determined from Eq. (23).

A parametric functional form involving components of secant stiffness tensor E'_{ijkl} and increment in the magnitude of strain tensor is proposed for P'^{f}_{ijkl}. The parametric form is given as

$$(P'^{f}_{ijkl})_{n+1} = \left(d_0^{ijkl}(P'^{f}_{ijkl})_n + \frac{(E'_{ijkl})_n}{d_1^{ijkl}(E'_{ijkl})_n + d_2^{ijkl}}\right)(\|e'_{ij}\|_{n+1} - \|e'_{ij}\|_n) \tag{26}$$

The coefficients d_1^{ijkl} and d_2^{ijkl} are found to depend on the secant stiffness as:

$$d_1^{ijkl} = -exp(d_3^{ijkl} - d_4^{ijkl}(E'_{ijkl})_n) - d_5^{ijkl}$$

$$d_2^{ijkl} = exp(d_6^{ijkl} - d_7^{ijkl}(E'_{ijkl})_n) - d_8^{ijkl} \tag{27}$$

The coefficients d_p^{ijkl} in Eqs. (26) and (27) are determined by nonlinear least squares minimization of the difference between results of micromechanical analysis for a few representative strain paths and those from the functional form. Fig. 4(b) shows that satisfactory fit is achieved for the components of P'^{f}_{ijkl} for a representative case of uniaxial tension.

5. Stress update algorithm for macroscopic analysis

The homogenization based continuum damage mechanics model is implemented for macroscopic finite element analysis using the user material interface (UMAT) in the commercial code ABAQUS. In an incremental solution process, subscripts n and $n + 1$ correspond to values at the beginning and end of the $n - th$ increment respectively. At each integration point of an element in the FE model, the stresses $(\Sigma_{ij})_{n+1}$ are obtained from known values of the strain $(e_{ij})_{n+1}$ and state variables at n using the HCDM constitutive model. The essential steps in the UMAT update algorithm for the $n - th$ increment are described below.

1. Given $(e_{ij})_{n+1}$, evaluate $(P'^{m}_{ijkl})_{n+1}$ using Eqs. (15) and (22) for monotonic loading and evaluate $(P'^{f}_{ijkl})_{n+1}$ using Eq. (26) for cyclic loading.

2. At the start of each iteration algorithm for solving the damage evolution problem, assume that the starting value of the PDCS rotation tensor $(Q_{ij})^{0}_{n+1} = (Q_{ij})_n$.

3. **Check for damage due to monotonic loading**: For the $I - th$ iteration, monotonic damage evolution takes place if:

$\frac{1}{2}(e'_{ij})_{n+1}(P'^{m}_{ijkl})_{n+1}(e'_{kl})_{n+1} - \kappa'_n > 0$. In this case, update the damage state variable as

$(\kappa'_{n+1})^I = \frac{1}{2}(e'_{ij})_{n+1}((P'^{m}_{ijkl})_{n+1})^I(e'_{kl})_{n+1}$ and proceed to step 6 to update the secant stiffness.

4. **Check for damage due to cyclic loading**: Evaluate the scalar product $\frac{\partial F'}{\partial e'_{ij}}\dot{e}'_{ij}$ or $P'^{f}_{ijkl}e'_{kl}\dot{e}'_{ij}$.

The applied load increment results in damage due to fatigue if:

$(P'^{f}_{ijkl})_{n+1}(e'_{kl})_{n+1}((e'_{ij})_{n+1} - (e'_{ij})_n) > 0$. In this case, update the damage state variable as

$$(\kappa'_{n+1})^I = \kappa'_n + \frac{1}{2}(e'_{ij})_{n+1}((P'^{f}_{ijkl})_{n+1})^I(e'_{kl})_{n+1} - \frac{1}{2}(e'_{ij})_n(P'^{f}_{ijkl})_n(e'_{kl})_n$$

and proceed to step 6 to update the secant stiffness.

5. **Unloading**: The applied load increment results in neutral loading or unloading if:

$F' < 0$ and $(P'^{f}_{ijkl})_{n+1}(e'_{kl})_{n+1}((e'_{ij})_{n+1} - (e'_{ij})_n) \le 0$. In this case, proceed to step 8 with unchanged secant stiffness tensor $(E_{ijkl})_{n+1} = (E_{ijkl})_n$.

6. Determine the secant stiffness as follows:

• Determine W_d by inverting the $\kappa' - W_d$ relation in Eq. (16) as

$$((W_d)_{n+1})^I = \frac{1}{b_2}\tan^{-1}\left(\frac{1}{b_1}\left(\frac{(\kappa'_{n+1})^I - b_0}{f_{n+1}(I_1, J_2, J_3)} - 1\right)\right) \tag{28}$$

- Using the backward Euler method to integrate $\dot{W}_d$, determine

$$(\lambda_{n+1})^I = \lambda_n + \frac{2(((W_d)_{n+1})^I - (W_d)_n)}{(e'_{ij} P'^{m/f}_{ijkl} e'_{kl})^I_{n+1}} \tag{29}$$

- Update the secant stiffness using the relation

$$(E'_{ijkl})^I_{n+1} = (E'_{ijkl})_n + (\lambda^I_{n+1} - \lambda_n)(P'^{m/f}_{ijkl})^I_{n+1} \tag{30}$$

7. Determine the PDCS rotation matrix $(Q_{ij})^I_{n+1}$ from the eigen-vectors of $(D_{ij})^I_{n+1}$, corresponding

to the updated secant stiffness $(E'_{ijkl})^I_{n+1}$ using the procedure described in section 2.1. If convergence in the rotation matrix is achieved, i.e.,

If max $|((Q_{ij})_{n+1})^I - ((Q_{ij})_{n+1})^{I-1}| \le TOL, \ \forall i, j = 1, 2, 3$

then proceed to step 8. Otherwise, return to step 3 and continue iteration.

8. Update macroscopic stresses with the converged value of the secant stiffness matrix $(E_{ijkl})_{n+1}$ as

$$(\Sigma_{ij})_{n+1} = (E_{ijkl})^I_{n+1}(e_{kl})_{n+1} \tag{31}$$

6. Numerical examples for validating the HCDM model

The orthotropic 3D homogenization based CDM (HCDM) model is validated by solving a few numerical examples. Results obtained from macroscopic simulations using the HCDM model are compared with homogenized micromechanical or HMM results for the RVE. The HMM model is obtained by homogenizing or volume averaging the micromechanical stresses and strains in the RVE subjected to periodic boundary conditions with imposed macroscopic strain as done in (Raghavan & Ghosh 2005). The macroscopic finite element model implementing the HCDM constitutive relations, consists of a single eight-noded quadrilateral element. A 3D fiber-matrix composite RVE consisting of a unit cube containing a cylindrical fiber of radius 0.2523 (Fig. 1) is considered for this validation study. Material properties of the elastic matrix are $E_m = 4.6$ GPa, $v_m = 0.4$, while for the elastic fiber they are $E_c = 210$ GPa, $v_c = 0.3$. The fiber volume fraction in the RVE is 20%. Cohesive zone parameters for the interface are $\delta_c = 5.0 \times 10^{-5}$ m, $\delta_e = 20 \times 10^{-4}$ m, $\delta_f = 20 \times 10^{-3}$ m and $\sigma_m = 0.02$ GPa. Micromechanical analyses of the RVE are conducted by enforcing periodic displacement boundary conditions and imposing the macroscopic strain fields on the RVE.

6.1 Model validation for monotonic loading

To validate the HCDMmodel for monotonic loading conditions, both proportional and non-proportional macroscopic strain loading conditions are applied as follows:

1. **L1** Proportional uniaxial tension loading: $e_{11} \neq 0$, all other $e_{ij} = 0$ for the entire loading process. This is taken as the reference loading path.
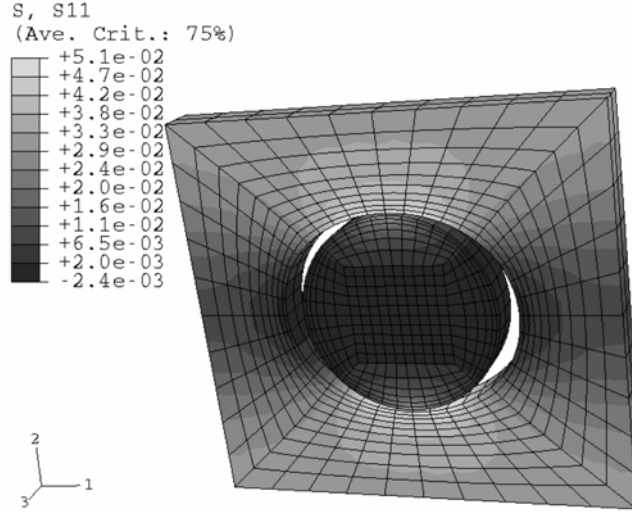
Fig. 5 Contour plot of microscopic stress (σ_{11}) in the RVE subjected to a uniaxial tensile strain $e_{11} = 0.004$

Table 1 Constants in the parametric representation of I_1, J_2 and J_3 in Eq. (15) for the single fiber RVE

A	B	c	F	G	H	L	M	N	O	P	Q	R	S
0.32	0.32	0.02	0.02	0.02	0.42	0.18	0.38	0.38	0.00	0.16	0.34	0.13	0.16

2. **L2** Proportional, combined tension/shear loading: $e_{11} \neq 0$, $e_{22} \neq 0$, $e_{12} \neq 0$, all other $e_{ij} = 0$ for the entire loading process.

3. **L3** Non-proportional loading: $e_{11} \neq 0$, all other $e_{ij} = 0$ (uniaxial tension in the first half of the loading); and $e_{11} \neq 0$, $e_{12} \neq 0$, all other $e_{ij} = 0$ (combined tension/shear in the second half of the loading)

Contour plot of the microscopic stress in the 3D RVE, subjected to uniaxial tension in the x_1 direction is shown in Fig. 5. The figure also shows the extent of debonding for the microstructure.

The various parameters in the HCDM model are calibrated for the RVE following the procedure outlined in section 4. The constants *A*, *B*, *C*, *F*, *G*, ..., *S* in Eq. (15) for the strain invariants are evaluated for the RVE and reported in Table 1. The constants exhibit symmetry with respect to x_1 and x_2 directions of the RVE. Since there are many calibrated constants in the expressions for κ' and P'^{m}_{ijkl}, only a few representative values are given. These are: $b_0 = 0.1E - 6$; $b_1 = 12.44$; $b_2 = 0.44E5$; $\alpha_0 = 0.42$; $\alpha_1 = 3.08$; $\alpha_2 = 2.44$; $\alpha_3 = 74.2$. For P'^{m}_{1111}, some of the constants are $c_0^{1111} = -1.16$; $c_1^{1111} = -0.144$; $c_2^{1111} = -0.615$; $c_3^{1111} = -0.144$

Figs. 6(a-c) compare the macroscopic stress-strain plots obtained from macroscopic analysis using HCDM with HMM results for the three load cases considered. The excellent match in most cases corroborates the satisfactory performance of the HCDM model. An important observation from these results is the sensitivity of the HCDM behavior to different loading conditions. The RVE subjected to loading (L1) shows rapid material degradation with increasing strain as the interface undergoes debonding in Fig. 6(a). The stiffness stabilizes at a strain of 0.0012 when the interface debonds completely. Similar trends are seen for the combined loading (L2) in Fig. 6(b), where
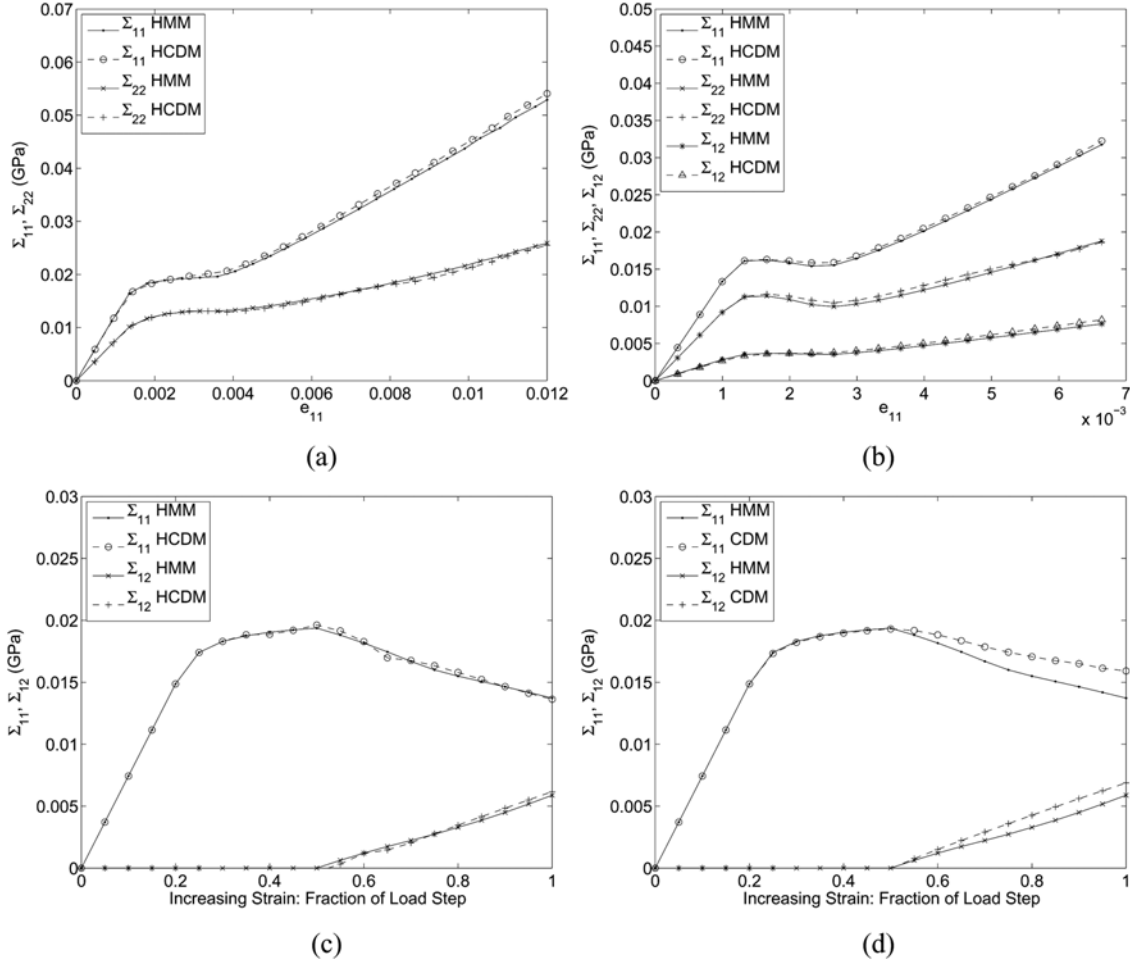
Fig. 6 Comparison of macroscopic stress-strain behavior obtained using HCDM and homogenized micromechanics (HMM) for RVE with a cylindrical fiber (Fig. 1), for load cases (a) L1, (b) L2, (c) L3 and (d) L3 without incorporation of PDCS

material degradation is followed by a constant stiffness phase corresponding to locked state. The merit of representing the HCDM model in the PDCS is evident from the results of the non-proportional loading case (L3) in Fig. 6(c). The PDCS representation results in a remarkable improvement of accuracy when compared to results in Fig. 6(d), which are obtained without incorporation of PDCS. The effectiveness of the HCDM model is evident from its CPU time of 20s, which is several times faster than that of HMM model with a CPU time of 780s.

6.2 Model validation for cyclic loading

The HCDM model is validated for cyclic loading by comparing the results of macroscopic simulations using the HCDM model with homogenized micromechanical or HMM results for the single fiber RVE. The RVE is subjected to cyclic tension-shear combined loading of $e_{ij} = \bar{e}_{ij} + \tilde{e}_{ij}$
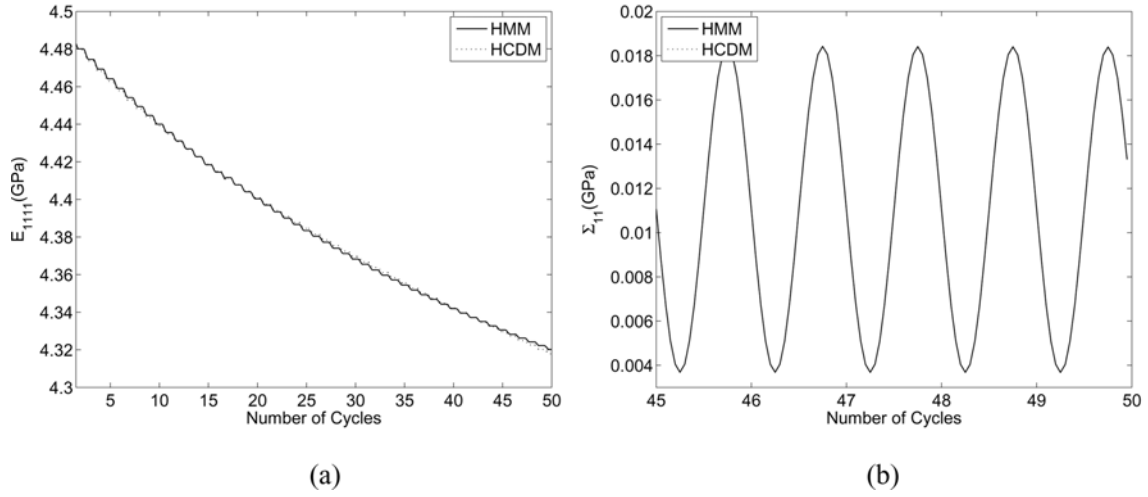
Fig. 7 Comparison of (a) component E_{1111} of elastic stiffness tensor and (b) macroscopic stress Σ_{11} obtained using HCDM and homogenized micromechanics (HMM) for RVE with a cylindrical fiber, for cyclic tension-shear combined loading of $e_{ij} = \overline{e}_{ij} + \widetilde{e}_{ij} \ \sin(2\pi t)$

$\sin(2\pi t)$. Figs. 7(a-b) show comparison of the HCDM predictions for stress and secant stiffness with the results of HMM for 50 cycles. Excellent agreement is obtained between HCDM and HMM in both cases. The components of elastic stiffness tensor degrade rapidly due to monotonic damage during the first cycle, followed by steady degradation due to fatigue damage. The CPU times for analyses with the HCDM and HMM models respectively, are 2 mins. and 175 mins. This reasserts the effectiveness of HCDM model.

The error in stresses predicted by the HCDM model in the above validation studies is attributed to the error in the functional representation of $\kappa'(W_d)$ and $P'^{m/f}_{ijkl}$, as well as the assumption of orthotropy. A rigorous sensitivity study is thereby conducted to ensure accurate representation of the damage parameters such as in Eqs. (22) and (26). Functional representations of Eqs. (16) and (22) have been successfully validated through tests on a variety of microstructural configurations and reported in Jain & Ghosh (2008b). It is evident from the examples discussed that the material degradation and consequently the variation of damage parameters depends on the applied strain path. This emphasizes the need for comprehensive 3D micromechanics based continuum damage model for use in macroscopic analysis modules.

7. Macro-micro analysis with the HCDM model

This section is intended to demonstrate the potential of HCDM model as a design tool for composite microstructures in structural applications by establishing a connection between macroscopic damage evolution and explicit microscopic failure mechanisms. Macroscopic structural simulation of damage evolution is conducted by the commercial FEM code ABAQUS (Abaqus 2001) with the HCDM model incorporated in the user subroutine UMAT. Once calibrated and validated, the HCDM model for a given RVE can be used for macroscopic analysis using the stress update procedure explained in section 5. A distinct advantage of the HCDM model over
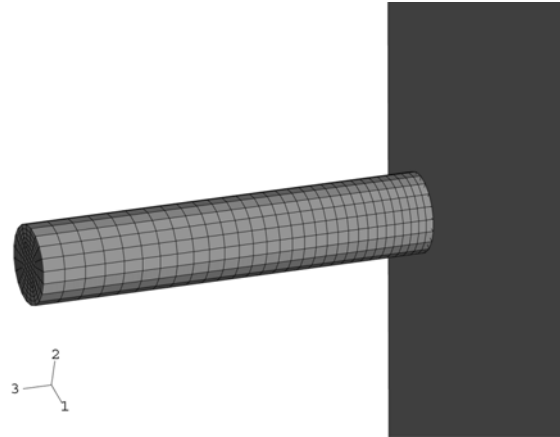
Fig. 8 Finite element model of a composite impactor colliding with a rigid surface

conventional macro-micro homogenization methods (Lene & Leguillon 1982, Guedes & Kikuchi 1991) is that the macroscopic analysis of large structures can be conducted very efficiently while preserving the effects of microstructural features.

7.1 Damage in projectile impact

The simulation involves a deformable composite projectile impactor colliding with a rigid surface as shown in Fig. 8. The impactor is cylindrical in shape with radius of 3.2 mm and length of 32.4 mm and is moving with initial velocity of 10 m/s. The impactor is assumed to be constituted of microstructural RVE described in section 6. The RVE is oriented in the structure such that the local (RVE) 3-direction coincides with the global 2-direction of Fig. 8. The macroscopic material behavior of the impactor is described by the calibrated HCDM model developed in section 4. To account for the inertia effects, the simulation is conducted with ABAQUS/Explicit with the HCDM constitutive law incorporated in VUMAT. The density of epoxy matrix is assumed to be 750 Kg/m^3 while that of steel fiber is 7800 Kg/m^3 so that, for fiber volume fraction of 20%, the density of the aggregate is 2160 Kg/m^3. The rigid surface and the projectile are modeled using continuum elements, and contact between projectile and rigid surface is assumed to be frictionless.

The total energy dissipated due to evolving damage (W_d) in the impactor is plotted as a function of time in Fig. 9(a). After initial period of elastic response corresponding to negligible values of total W_d, the damage initiates and W_d accumulates rapidly. Fig. 9(b) shows contour plot of energy dissipated W_d due to evolving damage at 5.0 μs. The damage initiates near the periphery of the impactor head and then propagates towards the center of the head cross-section. It is observed that at t = 5.0 μs (see Fig. 9(b)), damage is nonuniformly distributed about the center because of material orthotropy. The damage is seen to progress into the impactor as the stress waves due to impact travel into the impactor.

Time histories of the normal contact force at the impactor-rigid wall interface are compared in Fig. 10. The simulations are conducted with and without damage. The elastic stiffness tensor in the latter case is equal to the homogenized RVE stiffness with a perfect interface. The plots show that contact force rapidly reaches a peak value, reduces and stabilizes for a while and then gradually
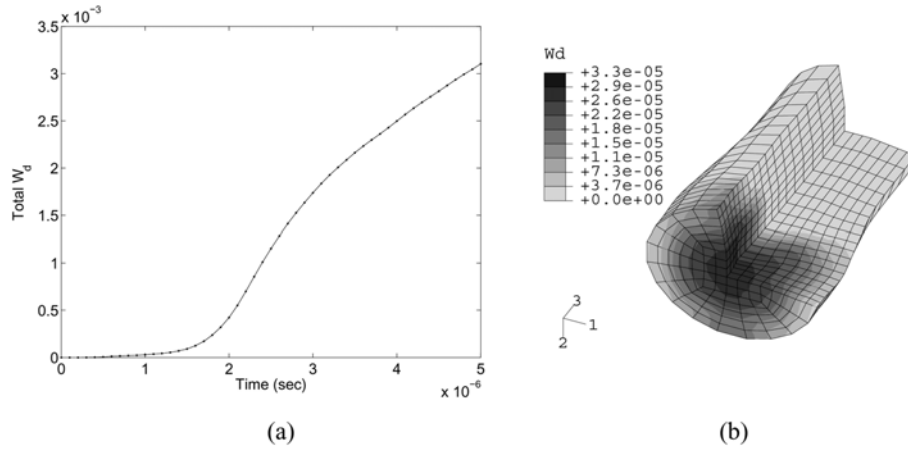
Fig. 9 Energy dissipated (W_d) due to evolving damage in the composite impactor (a) total W_d as a function of time and (b) contour plot of W_d at time = 5.0 μs
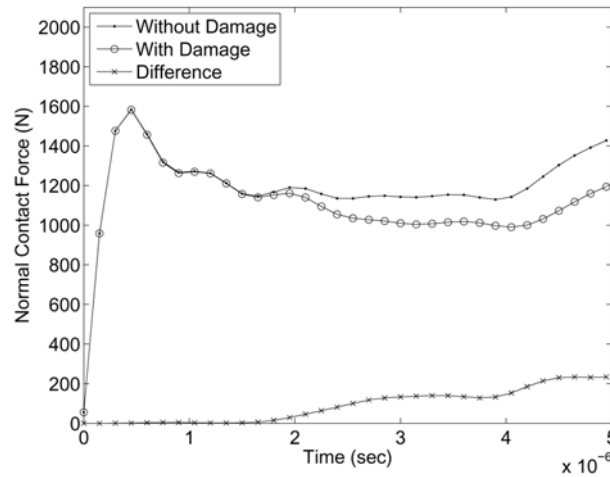

Fig. 10 Comparison of the interfacial contact force during impact with and without interfacial damage for composite impactor

increases again. Stress waves generated during impact propagate away from the center of impactor head towards the periphery. Also the waves propagate towards the back end of the impactor. Due to material orthotropy, the waves propagate at different speeds in different directions. The waves get reflected from the boundaries and interact with each other, causing the later increase in contact force. The contact forces with and without damage are concurrent until damage initiation, after which, the contact force with damage accumulation is lower. The difference between the two curves increases as more and more damage accumulates, indicating reduction in the load carrying capacity of the material.

Finally, the homogenization method allows for the assessment of stress-strain and damage evolution in the microstructural RVE, subject to a given macroscopic strain history. At a point on the
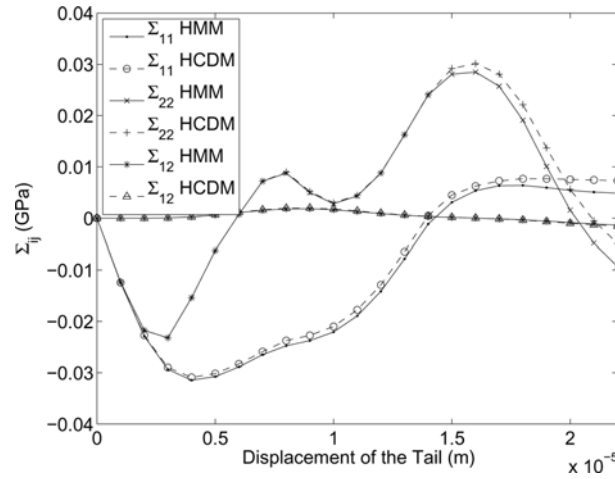
Fig. 11 Comparison of stress evolution predicted by HCDMmodel and the homogenized micromechanics (HMM) at a macroscopic point on the head of the composite impactor
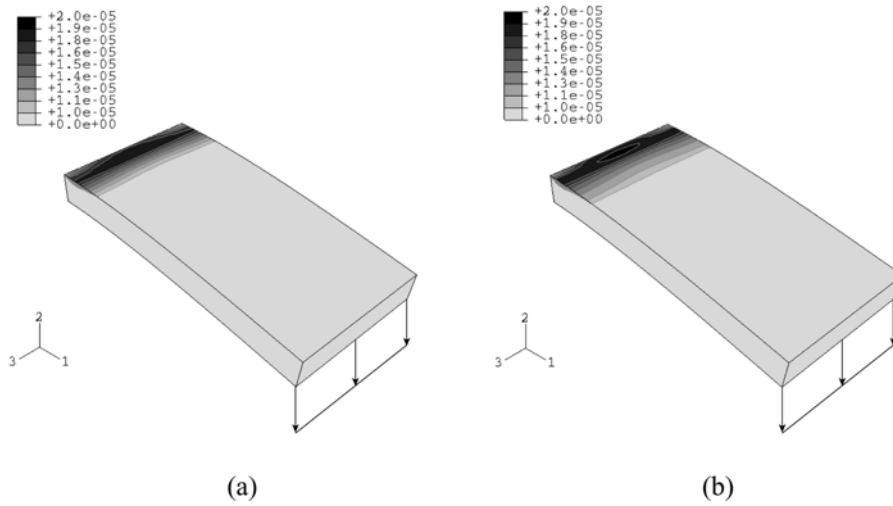

Fig. 12 Contour plots of energy dissipated (Wd) due to evolving damage for composite cantilever (a) after one cycle and (b) after 40 cycles

face of the impactor, the macroscopic stress evolution predicted by HCDM model is compared with the homogenized stress obtained from the microstructural RVE analysis subjected to macroscopic strain history. The comparison is demonstrated in the Fig. 11. Excellent agreement between the HCDM and the homogenized micro-scale distributions confirm the robustness of the HCDM model.

7.2 Fatigue damage in a composite cantilever

A composite cantilever thick plate of 5 m length, 2.5 m width and 0.5 m thickness is subjected to an oscillatory load at the free end as shown in Fig. 12. The cyclic behavior of the structure is simulated using ABAQUS/Standard. The plate is constituted of microstructural RVE as described in
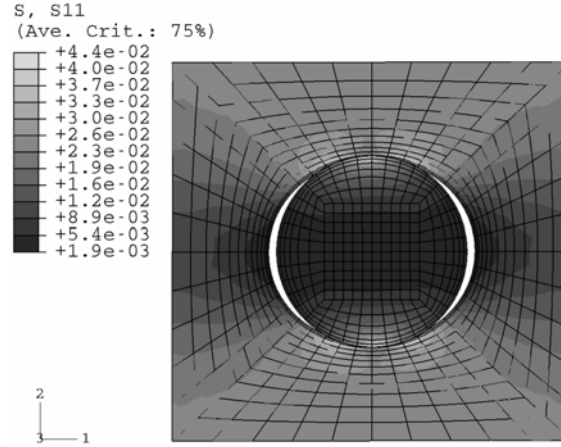
Fig. 13 Contour plot of the microscopic stress (σ_{11}) in the RVE at a macroscopic point on the top surface of the cantilever near the fixed end after 40 cycles
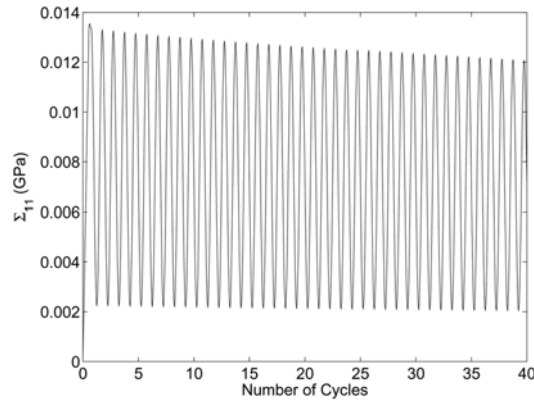

Fig. 14 Homogenized micromechanical stress Σ_{11} of RVE at a macroscopic point, showing steady reduction of the peak stress due to fatigue damage accumulation

section 6. The calibrated HCDM model developed in section 4 defines the constitutive behavior of the plate and is incorporated in ABAQUS user defined subroutine UMAT. A vertical displacement $u = \bar{u} + \tilde{u}\,\sin(2\pi t)$ is applied at the free end of the cantilever plate.

Figs. 12(a-b) show contour plots of the dissipated energy W_d due to evolving damage after one cycle and 40 cycles respectively. During the first cycle, the structure deforms elastically until high bending stresses cause damage to initiate at the top surface of the fixed end. The damage then accumulates rapidly till the end of the first cycle with the monotonic part of the loading. After the first cycle, the degraded material points undergo steady degradation due to fatigue. This is evident from the higher values of W_d in Fig. 12(b) compared to Fig. 12(a). Subsequently, redistribution of stresses takes place resulting in growth of damage zone as seen in the contour plots.

The damage evolution in the microstructural RVE can be assessed by subjecting the RVE to the macroscopic strain history at any material point. Fig. 13 shows the σ_{11} contour plot in the

microstructural RVE at a point on the top surface near the fixed end. The corresponding macroscopic stress evolution is shown in Fig. 14. The plot shows steady drop in the peak stress over the cycles because of fatigue damage accumulation.

8. Conclusions

An accurate and computationally efficient 3D homogenization based continuum damage mechanics model (HCDM) is developed for fiber reinforced composites undergoing interfacial debonding due to monotonic and cyclic loading. The HCDM model represents orthotropic behavior of damaging composites through a fourth order damage tensor which characterizes the stiffness as an internal variable. The effect of rotation of the principal damage axes due complex strain histories is accounted for by expressing the damage evolution laws in the principal damage coordinate system (PDCS). The model is found to accurately predict damage behavior for a wide range of proportional and non-proportional, monotonic as well as cyclic loading conditions. The proposed loading/unloading criterion for fatigue is seen to yield good accuracy. Functional forms of various damage parameters κ', P'^{m}_{ijkl} and P'^{f}_{ijkl} are developed in terms of the invariant forms I_1, J_2 and J_3 and stiffness tensor E'_{ijkl} to express variation of damage variables with the evolving damage. Parameters are calibrated by performing micromechanical RVE analysis for a few imposed strain histories. The functional forms of the parameters overcome the serious limitations of constant damage parameters that are conventionally assumed in CDM models. The assumption of orthotropy of damage laws in the PDCS is found to yield reasonably good accuracy. The model's robustness is evident from the good agreement between HCDM and homogenized micromechanical (HMM) response for a variety of loading paths. The capability of the model to efficiently predict damage in structures with explicit reference to the microstructural composition is demonstrated through macro-micro analysis of two composite structures. The ability of the HCDM model to directly correlate macroscopic behavior to the microstructural morphology, makes it a very effective tool in a material design framework to enhance the failure properties of structures.

Acknowledgements

References

Abaqus (2001). Users Manual. Hibbit, Karlsson and Sorensen, Inc.
Akshantala, N.V. and Talreja, R. (2000), "A micromechanics based model for predicting fatigue life of composite laminates", *Mat. Sci. Eng.*, A285.
Arnold, S.M. and Kruch, S. (1991), "A differential cdm model for fatigue of unidirectional metal matric composites", *NASA Technical Memorandum* 105726.

Bhatnagar, H., Walter, M E. and Ghosh, S. (2007), "A parametric domain map for top coat damage initiation and propagation in eb-pvd thermal barrier coatings", *Int. J. Multiscale Comput. Eng.*, **5**.

Bhattacharya, B. and Ellingwood, B. (1999), "A new cdm-based approach to structural deterioration", *Int. J. Solids Struct.*, **36**.

Chaboche, J.L. (1981), "Continuum damage mechanics: A tool to describe phenomena before crack initiation", *Nuclear Eng. Design*, **64**.

Chaboche, J.L., Kruch, S. and Pottier, T. (1998), "Micromechanics versus macromechanics: a combined approach for metal matrix composite constitutive modeling", *Eur. J. Mech. A/Solids*, **17**.

Chow, C. and Wang, J. (1987), "An anisotropic theory of elasticity for continuum damage mechanics", *Int. J. Frac.*, **20**.

Chow, C. L. and Wei, Y. (1999), "Constitutive modeling of material damage for fatigue failure prediction", *Int. J. Damage Mech.*, **8**.

Cordebois, J. and Sidoroff, F. (1982), "Anisotropic damage in elasticity and plasticity", *J. Mech. Theor. Appl.*.

Degrieck, J. and Paepegem, W.V. (2001), "Fatigue damage modeling of fiber-reinforced composite materials: review", *Appl. Mech. Rev.*, **54**(4).

Desmorat, R., Ragueneau, F. and Pham, H. (2007), "Continuum damage mechanics for hysteresis and fatigue of quasi-brittle materials and structures", *Int. J. Numer. Anal. Meth. Geomech.*, **31**.

Echle, R. and Voyiadjis, G.Z. (1999), "Simulation of damage evolution in a unidirectional titanium matrix composite subjected to high cycle fatigue", *Int. J. Fatigue*, **21**.

Feyel, F. and Chaboche, J.L. (2000). Fe2 multiscale approach for modelling the elastoviscoplastic behaviour of long fibre sic/ti composite materials", *Comput. Meth. Appl. Mech. Eng*, **183**.

Fish, J. and Yu, Q. (2002), "Computational mechanics of fatigue and life predictions for composite materials and structures", *Comput. Meth. Appl. Mech. Eng.*, **191**.

Fish, J., Yu, Q. and Shek, K. (1999), "Computational damage mechanics for composite materials based on mathematical homogenization", *Int. J. Numer. Meth. Eng.*, **45**.

Gathercole, N., Reiter, H., Adam, T. and Harris, B. (1994), "Life prediction for fatigue of t800/5245 carbon-fiber composites: I. constant amplitude loading", *Int. J. Fatigue*, **16**(8).

Ghosh, S., Bai, J. and Raghavan, P. (2007), "Concurrent multi-level model for damage evolution in microstructurally debonding composites", *Mech. Mater.*, **39**(3).

Guedes, J.M. and Kikuchi, N. (1991), "Preprocessing and post processing for materials based on the homogenization method with adaptive finite element methods", *Comput. Meth. Appl. Mech. Eng.*, **83**.

Hashin, Z. and Rotem, A. (1973), "A fatigue criterion for fiber reinforced composite materials", *J. Compo. Mater.*, **7**.

Jain, J.R. and Ghosh, S. (2008a), "Damage evolution in composites with a homogenization based contiuum damage mechanics model", *Int. J. Damage Mech.* (in press).

Jain, J.R. and Ghosh, S. (2008b), "Homogenization based 3d contiuum damage mechanics model for composites undergoing microstructural debonding", *J. Appl. Mech.*, **75**(3).

Ju, J.W., Ko, Y.F. and Ruan, H.N. (2006), "Effective elastoplastic damage mechanics for fiberreinforced composites with evolutionary complete fiber debonding", *Int. J. Damage Mech.*, **15**(3).

Kachanov, L. (1987), *Introduction to Continuum Damage Mechanics*. Dordrecht, Boston, M. Nijhoff.

Kouznetsova, V., Brekelmans, W.A.M. and Baaijens, F.P.T. (2001), "An approach to micro-macro modeling of heterogeneous materials", *Comput. Mech.*, **27**.

Krajicinovic, D. (1996). *Damage mechanics*. Elsevier, Amsterdam.

Kruch, S., Carrere, N. and Chaboche, J.L. (2006), "Fatigue damage analysis of unidirectional metal matrix composites", *Int. J. Fatigue*, **28**.

Ladeveze, P. (2002), "An anisotropic damage theory with unilateral effects: Applications to laminates and to three- and four-dimensional composites", *Cont. Damage Mech. Mater. Struct.* eds. O. Allix and F. Hild, 1.

Lene, F. and Leguillon, D. (1982), "Homogenized constitutive law for a partially cohesive composite material", *Int. J. Solids Struct.*, **18**(5).

Li, S. and Ghosh, S. (2004), "Debonding in composite microstructures with morphologic variations", *Int. J. Comput. Methods*, **1**(1).

Marigo, J.J. (1985), "Modeling of brittle and fatigue damage for elastic material by growth of microvoids", *Eng.*

Frac. Mech., **21**(4).

Murakami, S. (1988), "Mechanical modeling of material damage", *J. Appl. Mech.*, **55**.

Pellegrino, C., Galvanetto, U. and Schrefler, B.A. (1999), "Numerical homogenization of periodic composite materials with non-linear material components", *Int. J. Numer. Meth. Eng.*, **46**.

Raghavan, P. and Ghosh, S. (2005), "A continuum damage mechanics model for unidirectional composites undergoing interfacial debonding", *Mech. Mater.*, **37**(9).

Reifsnider, K.L. (1987), "Life prediction analysis: directions and divagations", *Proc. 6th Int. Conf, Composite Mater.*, **4**.

Rosek, J. and Onate, E. (2008), "Multiscale analysis using a coupled discrete/finite element model", *Interaction Multiscale Mech., An Int. J.*, **1**(1).

Sidoroff, F. and Subagio, B. (1987), "Fatigue damage modeling of composite materials from bending tests", *Proc. 6th Int. Conf. Composite Mater.*, 4.

Simo, J.C. and Ju, J.W. (1987), "Strain and stress-based continuum damage models, part I: Formulation", *Int. J. Solids Struct.*, **23**(7).

Suresh, S. (1996), *Fatigue of Materials*, Cambridge University Press, Cambridge.

Swaminathan, S., Pagano, N.J. and Ghosh, S. (2006), "Analysis of interfacial debonding in threedimensional composite microstructures", *J. Eng. Mater. Tech.*, **128**.

Talreja, R. (1987), *Fatigue of Composite Materials.*, Technomic Pub. Co.

Voyiadjis, G.Z. and Kattan, P.I. (2006), *Advances in damage mechanics*: *Metals and metal matrix composites with an introduction to fabric tensors*. Elsevier.

Whitworth, H.A. (1998), "A stiffness degradation model for composite laminates under fatigue loading", *Compos. Struct.*, **40**(2).